

# Flow analysis on the ventral gap of a paper airplane

Min Chang<sup>1</sup>, Xiaoyu Feng<sup>2</sup>, Yang Zhang<sup>3</sup>, Xu Zhang<sup>3</sup> and Junqiang Bai<sup>1</sup>

Proc IMechE Part C:  
J Mechanical Engineering Science  
0(0) 1–10  
© IMechE 2020  
Article reuse guidelines:  
sagepub.com/journals-permissions  
DOI: 10.1177/0954406220946076  
journals.sagepub.com/home/pic



## Abstract

It is a challenging work to design micro aerial vehicle with great aerodynamic performance because the tiny wingspan at low-Reynolds-number cannot provide lift efficiently. The aerodynamic configuration of a classic delta-wing paper airplane is investigated in the present work with numerical method to discover its potential for micro aerial vehicle designs. Furthermore, the effect of the ventral gap on the aerodynamic characteristics of the paper airplane is investigated herein. The stall angles of attack reach  $37.5^\circ$  and  $40^\circ$ , respectively, for ventral opened configuration and the closed one, and the maximum lift coefficient reaches 1.49 and 1.46. The ventral-opened configuration has negative pitching moment coefficient ( $-0.01431$ ) even at  $37.5^\circ$  while the closed one has a positive coefficient ( $0.01402$ ). The reason may be the gap leads to a strong back-flow vortex before the trailing edge in the ventral gap which produces a strong nose-down moment. Generally, the ventral gap improves lift and dramatically influences the longitudinal stability compared with the one without it.

## Keywords

Micro aerial vehicle, low Reynolds-number flow, paper airplane, ventral gap, computational fluid dynamics

Date received: 3 April 2020; accepted: 7 July 2020

## Introduction

In recent years, micro aerial vehicle (MAV) has gradually gained lots of attention due to its advantages, such as light weight, more portable, stealthier and cost-effective, and flies higher than conventional aerial vehicles. MAV flies at low-Reynolds-number condition, in which the airflow dynamics of aircraft is quite different from that at high Reynolds number. For example, the viscous effect of the air at low-Reynolds-number condition is more serious which will bring higher drag and lower lift.<sup>1,2</sup> It also makes the wing easier to stall because of the air separation. Therefore, the experience and methods obtained from the flow at high Reynolds number may not be applicable to MAVs.<sup>3</sup> Many researches focus on the designing aerial vehicles, which can be used in the low-Reynolds-number flow, via being inspired by the wing structures of birds and insect.<sup>4,5</sup> This process, however, is still slow due to the complicated mechanism of birds and insect fly.

As flying at a similar range of Reynolds number with MAV, the paper airplane has been tested and improved with trial-and-error due to its low cost and easiness to be produced. Nevertheless, no work has been done to prove that the mostly used configuration, i.e. delta wing with a ventral gap, has its own

advantages compared with conventional aircraft configurations. Torres et al.<sup>6</sup> performed an experiment to study the aerodynamic performance of low aspect ratio wings made by flat plate with several Reynolds number; they found the maximum lift coefficient of conventional wings had difficulty to exceed 0.75 under a Reynolds number of 70,000. Paper airplanes, however, inheriting the advantage of delta-wing configuration, can bring strong leading-edge vortices, which can enhance the lift obviously.<sup>7</sup> Experiment results show that a paper airplane like MAV with a sweep angle of  $75^\circ$  can provide a maximum lift coefficient of up to 1.4 under a Reynolds number of 75,000,<sup>8</sup> which is much larger than that of a conventional wing (0.75).

<sup>1</sup>Unmanned System Research Institute, Northwestern Polytechnical University, Xi'an, China

<sup>2</sup>School of Aeronautics, Northwestern Polytechnical University, Xi'an, China

<sup>3</sup>State Key Laboratory for Strength and Vibration of Mechanical Structures, Xi'an Jiaotong University, Xi'an, China

## Corresponding author:

Chang Min, Unmanned System Research Institute, Northwestern Polytechnical University, No. 127 Youyi Road, Xi'an, China.  
Email: changmin@nwpu.edu.cn

In the field of airflow upon delta wing at low Reynolds number, several works exist. Kegelmann and Roos<sup>9</sup> found the characteristics of separation at the leading edge and the strength of the leading-edge vortex are the important factors determining vortex lift. Dickinson et al.<sup>10</sup> showed how the unsteady process of vortex generation at large angles of attack contributes to the production of aerodynamic forces in insect flight in 1993. It says that impulsive movement at high angles of attack resulted in the production of a leading-edge vortex, which brings a dramatic increment in lift.

In 2001, Mitchell and Delery<sup>11</sup> present that the formation of the primary vortex is only slightly dependent on the Reynolds number, while secondary and tertiary vortices are, however, Reynolds number dependent. Then, Ol and Gharib<sup>12</sup> found that with increasing angle of attack, the slender delta wing exhibits the usual jet-like axial velocity profile of stable primary LE vortices, whereas the non-slender wing fails to have a significant axial velocity peak even for conditions devoid of identifiable vortex breakdown. In 2004, Torres and Mueller<sup>13</sup> found that the location of the center of lift shifted toward the trailing edge of the wing as the angle of attack increased which is related to the nonlinear lift generated by the wing-tip vortices through wind tunnel tests. In 2010, Kwak and Nelson<sup>14</sup> researched the vortical flow control over delta wings with DBD plasma actuators. After that, Shen et al.<sup>15</sup> researched the asymmetric flow control on delta wings.

All works above and others did great contribution to the research about the airflow upon delta wing at low Reynolds number. However, we find that almost all works of them are based on the flat delta plates. However, when we focus on the configuration of paper airplane, we cannot neglect the influence of the ventral gap at the centerline of the airplane.

Schlüter<sup>16</sup> has made force measurement and flow field display through water tunnel experiments, and concluded that the ventral gap of paper airplane has influence on aerodynamic performance. They also

made an abbreviated explanation of the influence from the aspect of spatial vorticity distribution through numerical simulation using LES methods, but the analysis is not further enough.

In this paper, we first verify the experiments performed by Schlüter<sup>16</sup> through numerical simulation. Then some analyses are made on the flow mechanisms at some classic angles of attack. Finally, the way how the ventral gap of blend-dart paper airplane affects the flight performance is studied.

## Model construction, description of symbols

### Paper airplane model

The configuration we use in this study adopts the configuration of experimental model provided in Schlüter,<sup>16</sup> which is a common delta wing configuration of paper airplane. The model can be obtained using a piece of A4 paper following the procedure seen in Figure 1. The size of the airplane is the same as the model provided in the reference.

### Coordinates system and symbol description

We declare that the origin of coordinates lies at the nose point of the airplane, and the XOZ plane is the symmetry plane of the airplane. Facing forward of the airplane as a thrower, the X-axis is parallel to the line connecting the nose and the trail of the airplane, taking head-trail direction as positive; the Y-axis is perpendicular to the symmetric plane, taking the right side of the thrower as positive; and the Z-axis satisfies the right-hand rule, which means we take upward direction as positive.

The symbols used in this paper are defined as follows:  $AOA$  refers to the angle of attack of the airplane,  $C_L$  refers to lift coefficient,  $C_D$  refers to drag coefficient,  $K$  refers to lift to drag ratio,  $C_m$  refers to pitching moment coefficient,  $C_p$  refers to pressure coefficient, and  $X$  vorticity refers to vorticity along X-axis.

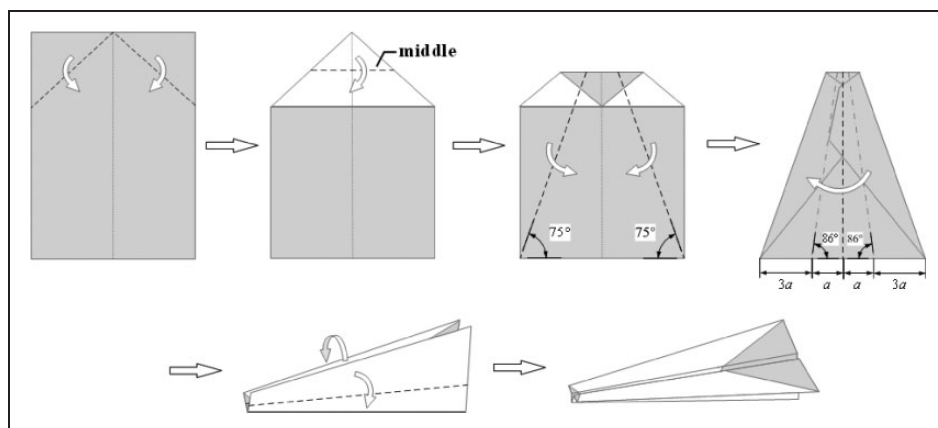


Figure 1. Folding procedure to obtain the blend-dart paper airplane.

## Calculation method and credibility verification

### Calculation method

In this paper, the Reynolds Average Navier-Stocks (RANS) is used as governing equation, and it is given as

$$\frac{\partial Q}{\partial t} + \frac{\partial(F - F_v)}{\partial x} + \frac{\partial(G - G_v)}{\partial y} + \frac{\partial(H - H_v)}{\partial z} = 0 \quad (1)$$

The finite volume method based on the finite element method is adopted to solve the equation. It not only ensures the conservation properties of the finite volume method but also absorbs the accurate merit of the finite element method. To close the new stress terms resulted from Reynolds Average, the Menter's  $k-\omega$  SST turbulence model is adopted.<sup>17,18</sup> This model uses  $k-\omega$  model within the boundary layer, while uses  $k-\varepsilon$  model on the edge of boundary layer and within exterior free shear layer, a mixed function is used for the transition; thus, this model is two-equations viscous model. The Menter's  $k-\omega$  SST turbulence model eliminates the dependence of  $k-\omega$  model on far-field boundary conditions, and at the same time improves the accuracy of  $k-\varepsilon$  model on the simulation of large adverse pressure gradient.<sup>19</sup> Although some high precision method<sup>20</sup> will get a better result, it will also bring pretty high computational costs. Lots of Abundant practices reveal that the Menter's  $k-\omega$  SST model can accurately simulate the complex flows such as separation flow, vortex flow in the aviation and astronautics field.<sup>21</sup>

### Calculation credibility verification

To verify the credibility of the calculation method used in this paper, two models, named Model 1 (Ventral-closed configuration) and Model 2 (Ventral-opened configuration) as shown in Figure 2(a), are constructed for simulation. The two models are based on the models used for water tunnel experiments in Schluter<sup>16</sup> and can be obtained by folding a piece of A4 paper following the procedure given in

Figure 1. The geometries of the paper plane models are as shown in Figure 2(b). The paper plane has a swept angle of  $75^\circ$ . The root chord length is 250 mm. The force measurements are managed in a water tunnel with a test section size 0.3 m wide  $\times$  0.3 m high  $\times$  1.0 m long. The flow uniformity is about 1% and the turbulence intensity is below 1% at water flow speed of 0.6 m/s. An external three-component force balance is used to measure the forces. The maximum absolute error is 0.1 N at the full load of 20 N. Models are tested at Reynolds number of 75,000.<sup>16</sup>

In the computational fluid dynamics (CFD) calculation, unstructured grids are adopted, the surface of the airplane is set as wall without sliding, and the far field and symmetrical conditions are also set as normal conditions. To ensure a fair comparison, the two configurations adopt similar grid volume and density. The size of the first layer normal to the wall is  $2.5 \times 10^{-5}$  ( $y^+ < 1$ ), with a growth rate of 1.2. The total grid volume of the whole flow field is 8 million. To make a better comparison, the simulating condition is set as the water tunnel tests. The fluid material is set as water and the Reynolds number of the simulation is 75,000. The grid formation of the two configurations and the comparison between the simulation results and testing results of  $C_L$  are shown in Figure 3.

It can be seen from the figure that the computed  $C_L$  has a relatively linear increase before  $20^\circ$ , and the increase gets leveled around  $35^\circ$ , followed by a soft stall at  $AOA$  about  $40^\circ$ . The maximum  $C_L$  of both is around 1.5, while in the water tunnel tests the  $C_L$  of configuration with a ventral gap reaches 1.7. The calculation results agree well with the testing ones with a maximum error of 15%, and although the advantage of the ventral gap may be under-estimated, the trends are correct and instructive enough. In addition, the agreement is more satisfactory among the low  $AOAs$ , which is  $0-20^\circ$ . It can be concluded that the calculation method used for the configuration of paper planes with large sweep angles at low Reynolds numbers is relatively credible for the study in this article.

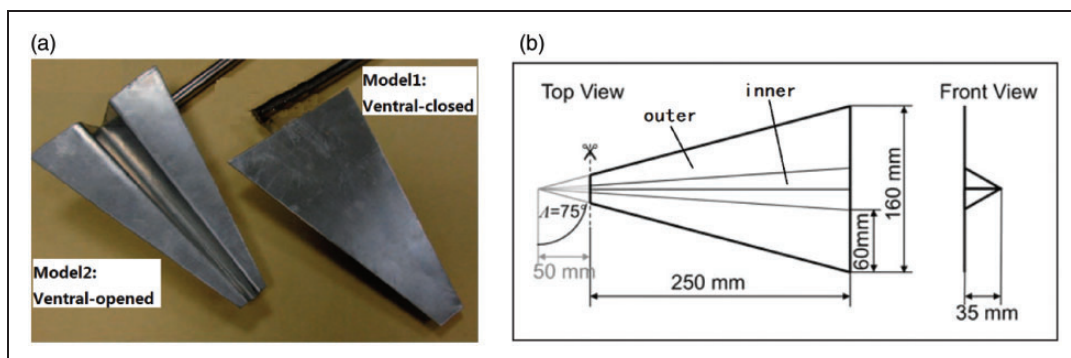


Figure 2. Test models and actual dimensions mentioned in Schluter.<sup>16</sup>

## The influence of the ventral gap type: Opened or closed

### Lift coefficient and drag coefficient

The paper planes with high sweep angles usually have large stall  $AOAs$ .<sup>3,22</sup> As shown in Figure 3, the stall  $AOAs$  reach  $37.5^\circ$  and  $40^\circ$ , respectively for ventral opened configuration and the closed one. The maximum  $C_L$  reaches 1.49 and 1.46. Therefore, the paper planes with and without the centerfold have some differences in aerodynamic characteristics. For better understanding, two  $AOAs$  (i.e.  $20^\circ$  and  $37.5^\circ$ ) are selected to explore the flow features. The force is integrated by airplane parts, and two configurations share the same reference areas for better comparing. The obtained  $C_L$  can be seen in Figure 4, in which the “inner part” refers to the ventral gap part, and the “outer part” refers to the outer wing part as shown in Figure 2(b). It is obvious that the difference in  $C_L$  of the two configurations mainly results from outer

parts. Within the limits of the  $AOAs$  we study, the two parts of the ventral-opened configuration always provide more lift than those of the ventral-closed configuration. Besides, the reference area ratio of outer part and inner part is almost 3:1, and it is significantly lower than the  $C_L$  ratio ( $\approx 6:1$ ) shown in Figure 4, which means the outer part may produce lift more efficiently.

The spatial vorticity distribution contours of the two configurations at the two  $AOAs$  are shown in Figure 5, in which the slices are chosen at  $X = 0.01\text{ m}$ ,  $0.03\text{ m}$ ,  $0.06\text{ m}$  and  $0.1\text{ m}$ , respectively. In Figure 5, (a) and (b) are the contours of two configurations at  $AOA$  of  $20^\circ$ , and (c) and (d) are the contours at  $AOA$  of  $37.5^\circ$ . It can be seen from (a) and (b) that at the  $AOA$  of  $20^\circ$ , the vorticity distribution shows no obvious difference for the two configurations, except for the slice at  $X = 0.01\text{ m}$ , where there is stronger vorticity for the ventral-opened configuration than the closed one in the inner part. It may

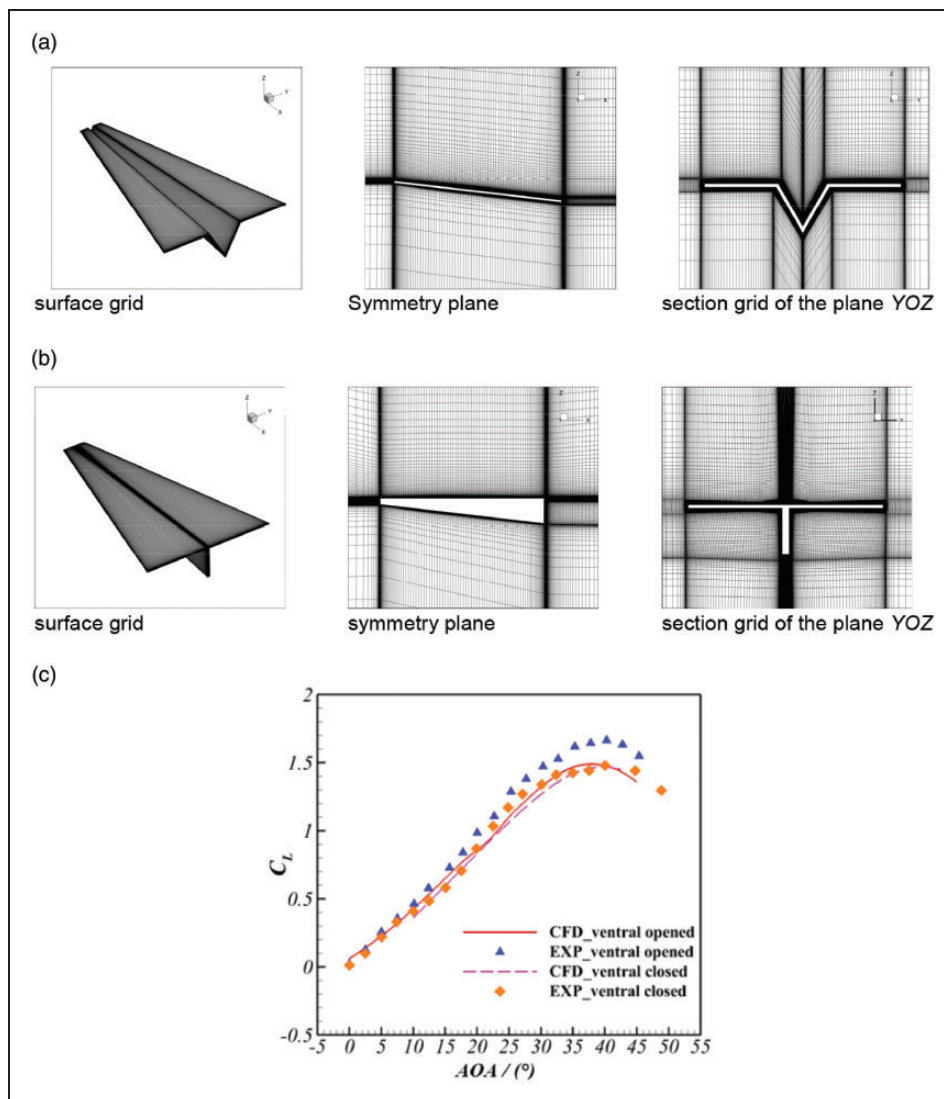


**Figure 3.** Distribution of grids of the two configurations and the comparison between computational fluid dynamics simulation results and experiment results.



be caused by the V-type ventral gap of the ventral-opened configuration, because of which the inner part has a bigger local  $AOA$ , and gets stronger vorticity. At the  $AOA$  of  $37.5^\circ$ , as shown in (c) and (d), the ventral-closed configuration has stronger vorticity at  $X=0.06\text{ m}$  and  $X=0.1\text{ m}$ .

Figure 6(a) is the  $Q$  criterion contours of the two configurations at the  $AOA$  of  $37.5^\circ$ , and the value  $Q$  shown in the figures refers to the  $Q$  Criterion. The slice positions are the same as those in Figure 5

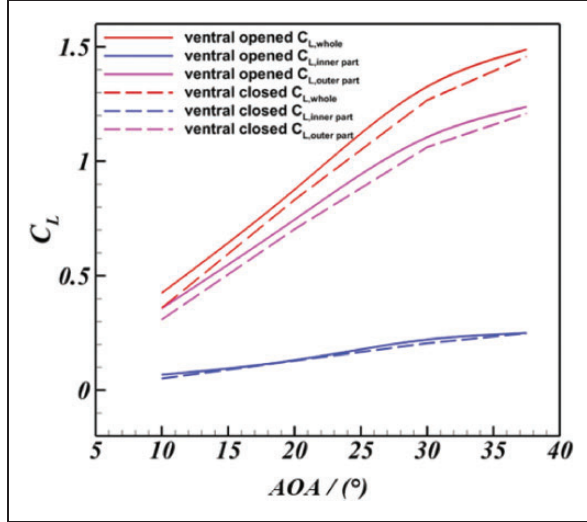


**Figure 4.** Comparison of force integrated by paper plane parts.

except the first slice which lies at  $X=0.005\text{ m}$  in Figure 6(a). An interesting phenomenon can be discovered from Figure 6 (a) that turbulence generates in the ventral gap of the ventral-opened configuration around  $X=0.005\text{ m}$  and  $X=0.1\text{ m}$ , which are the most forward and backward slice as shown in Figure 6(a). Figure 6(b) shows the streamlines and pressure distribution at the symmetric plane of two configurations. It can be seen that for the ventral-opened configuration, the free stream experiences strong backflow vorticity after passing the nose. Similar to the analysis before, the vorticity is stronger than the ventral-closed configuration as it has larger local  $AOA$ .

A down-wash flow exits after the vorticity because of the strong entrainment effect, and between the vorticity and the down-wash flow there lies a dead water area where acts as a high-pressure zone in Figure 6(b). The down-wash flow flows to the trail after impacting the paper plane's upper surface and produces another backflow after encountering the high-pressure area near the trailing edge. The backflow vortex here restrains the high-pressure zone from moving forward on the upper surface to some extent. The reason may be the vortex here will induce the high-momentum flow into the boundary layer, and hence enhances the capability of the boundary layer to withstand the adverse-pressure gradient. Different from the phenomenon discussed above, the ventral-closed configuration shows no significant indications of the backflow at the trailing edge. The reason may be the

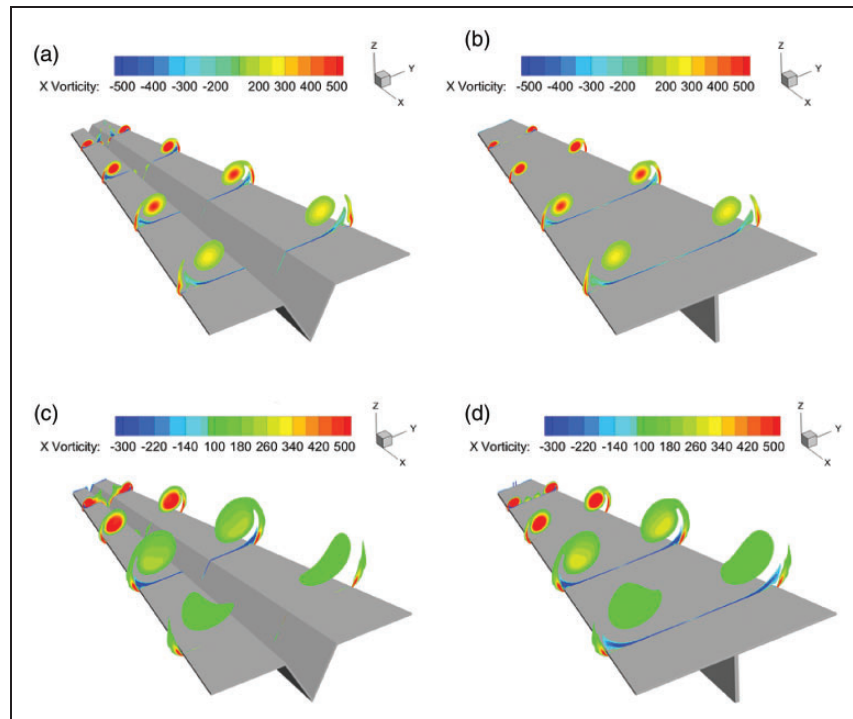


**Figure 5.** The spatial vorticity distribution contours under Alpha  $20^\circ$  and  $37.5^\circ$ .

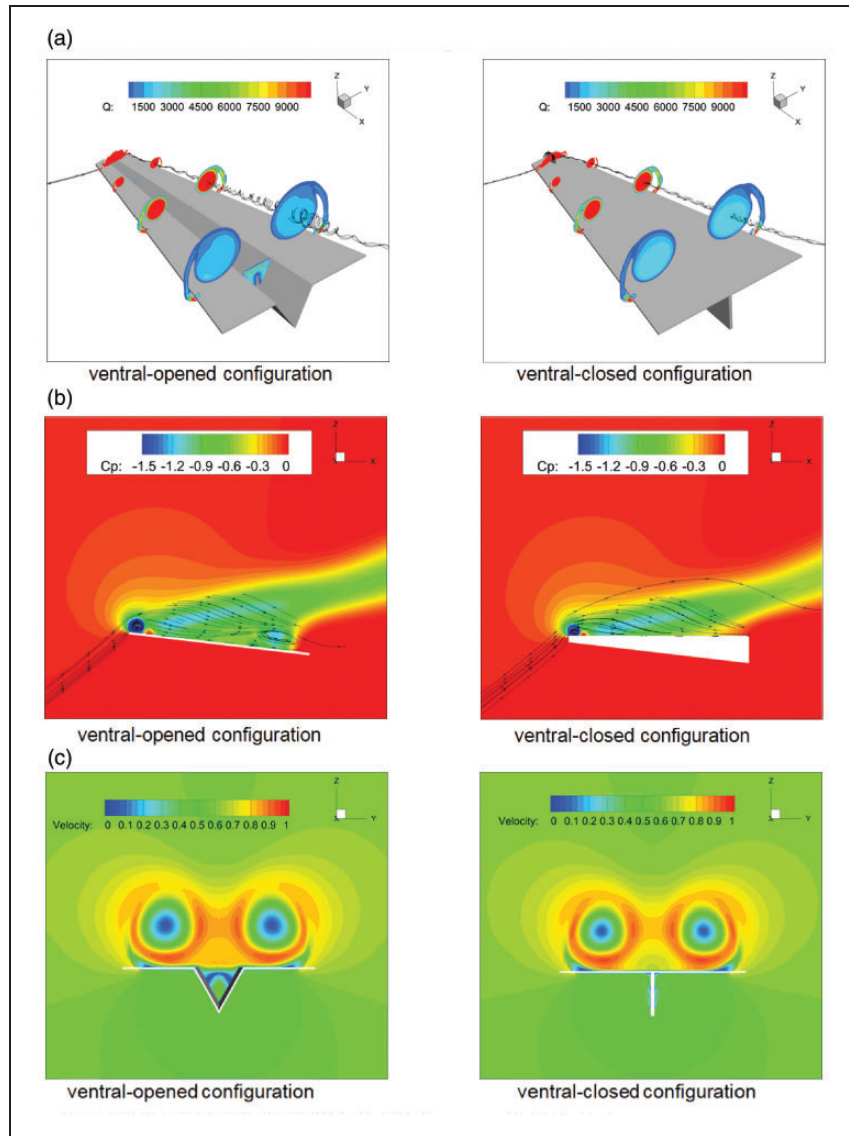


**Figure 6.** Q criterion contours, spatial streamline and pressure distribution (asymmetrical plane), and spatial flow velocity distribution ( $X=0.1$  m) at  $AOA$  of  $37.5^\circ$ .

V-type ventral gap makes the first vortex stronger as introduced before which induces a stronger down-wash flow and provides a spatial condition for the flow to 'jump' after impacting the upper surface. These two reasons make the flow over ventral-opened configuration easier to be rolled up than ventral-closed configuration under the high pressure near the trailing edge. The influence of these phenomena on the surface pressure distribution will be explained next.

Figure 6(c) shows the airflow velocity distribution of two configurations at  $X=0.1$  m with the  $AOA$  of  $37.5^\circ$ . From the figure it can be seen that the velocity distribution at the ventral gap of the ventral-opened configuration agrees well with the backflow vortex here. As seen in Figure 6(a) and (b), the flow generates a strong back-flow vortex near the trailing edge. At the vortex core, flow speed will decline to about 0,

which is shown with blue area within the ventral gap in Figure 6(c). What's more, the backflow also speeds up the airflow between the two vortices above the ventral gap. This behavior will retard the shear between flows with different velocity and slow down the flow deceleration, which can be seen in Figure 6(c) above the ventral gap. This high-speed airflow will benefit the lift of the paper plane.

Then we present the stream-wise pressure distribution at slices of  $Y=0$  m,  $Y=0.01$  m,  $Y=0.02$  m and  $Y=0.03$  m with the  $AOA$  of  $37.5^\circ$  in Figure 7, and the span-wise pressure distribution at slices of  $X=0.01$  m,  $X=0.03$  m,  $X=0.06$  m and  $X=0.1$  m in Figure 8. Distributions of these slices are listed in the order mentioned above. From Figure 7 we can find that the ventral-opened configuration has two low-pressure zones above the upper surface at the symmetrical plane, one of which lies at the nose and the other lies

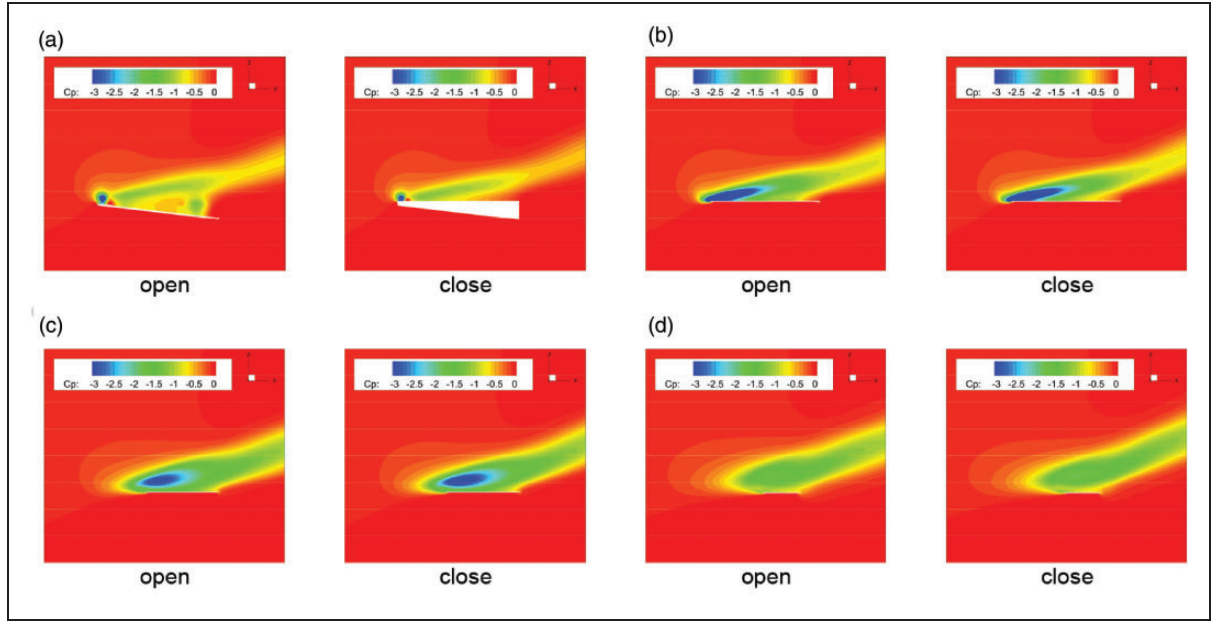


**Figure 7.** Stream-wise pressure distribution contours of two configurations with the AOA of  $37.5^\circ$  (“open” means ventral-opened configuration, “close” means ventral-closed configuration).

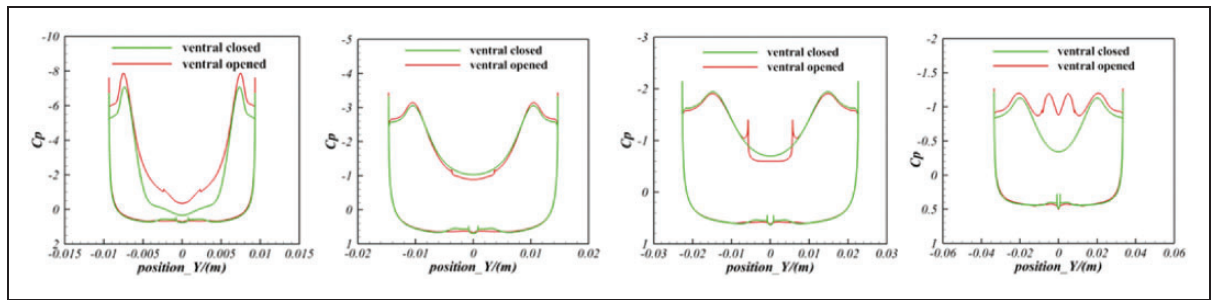


**Figure 8.** Span-wise pressure distribution of the two configurations with the AOA of  $37.5^\circ$ .

before the trailing edge. Both of them correlate well with the backflow we mentioned before. Also, we find that the low-pressure zone at the front part is stronger than that of the ventral-closed configuration, which may be caused by the stronger vortex as we analyzed before. From the rest Y slices in the contours, it can be seen that two configurations have similar pressure distribution near the leading edge but the ventral-opened configuration has a larger area of low pressure near the trailing edge, which is especially obvious above the ventral gap. This larger low-pressure area is mainly due to the second back-flow vortex, and it contributes a lot to the lift over the paper plane. Meanwhile, it also leads to some pitching moment benefits, which will be discussed later.

The characteristics discussed above are reflected in Figure 8, too. For example, the ventral-opened configuration has lower pressure on the upper surface at  $X=0.01$ , and the difference mainly centers on the inner part, which is the area that the first backflow vortex exits. For  $X=0.1$  m that is close to the trailing edge, the ventral-opened configuration has slightly

stronger low pressure over the outer part, while it also produces a notably higher low-pressure zone over the inner part, because of the trailing edge back-flow vortex.

Table 1 shows the drag coefficients ( $C_D$ ) of the inner part and outer part, respectively. From the table it can be seen that the ventral-opened configuration has larger  $C_D$  at both AOA. At AOA of  $20^\circ$  the difference is 0.0307, and at  $37.5^\circ$  the difference is 0.065. At AOA of  $20^\circ$ , the inner part and outer part contribute equally to the difference at  $20^\circ$  (around 0.015). However, the inner part contributes 0.0202 larger of difference at AOA of  $37.5^\circ$ . By taking the analysis above into account, we know that the ventral-opened configuration has two obvious backflow vortices at the nose and the trail of the inner part, resulting in large negative pressure zones at  $37.5^\circ$ . This may bring large pressure-induced drag. Moreover, higher local velocity near the up surface caused by the vortex may also lead to higher  $C_D$ , so that the ventral-opened configuration has a larger increment in  $C_D$  at the AOA of  $37.5^\circ$ .

**Table 1.** Drag coefficients by parts of the two configurations.

AOA (°)	20			37.5		
Configuration	Open	Close	Difference	Open	Close	Difference
Inner part $C_D$	0.07421	0.05928	0.01493	0.24778	0.20518	0.04260
Outer part $C_D$	0.27844	0.26267	0.01577	0.94021	0.91781	0.02240
Total $C_D$	0.35264	0.32194	0.03070	1.18799	1.12299	0.06500

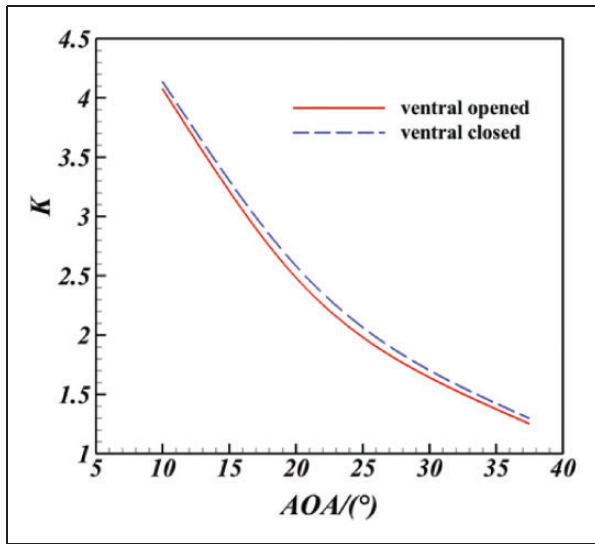
**Figure 9.** Lift to drag ratio curves.

Figure 9 presents the comparison between two configurations on the lift to drag ratio ( $K$ ). It is obvious to see that the ventral-opened configuration has larger  $C_L$  but smaller  $K$  at all  $AOAs$  we discuss. The weakness of the ventral-opened configuration in  $K$  may be caused by the higher drag we discussed before. Higher lift is accompanied by higher drag, and the drag increases more. Therefore, in practice, the configuration should be chosen based on the tradeoff of the  $C_L$  and  $K$ .

### Pitching moment coefficient

Table 2 provides the pitching moment coefficient ( $C_m$ ) of the inner part and the outer part. Based on measured data, the center of gravity of the ventral-opened configuration is at the center point of the root chord, which is at  $X = 0.0625$  m. We take it as reference point for calculating the  $C_m$  as shown in the table.

Figure 10(a) is the comparison of pitching moment coefficient for two configurations. It can be seen that the pitching moment of ventral-closed configuration is consistent with our common understanding, which can be explained by the forward movement of the vortex burst location. However, for the ventral-opened configuration, the slope of the pitching moment coefficient curve reverses twice at  $AOA = 18^\circ$  and  $30^\circ$  after it is unstable. This

phenomenon may be explained by the change of both the back-flow vortex and the leading-edge vortex. The enhancement of the back-flow vortex provides more nose-down moment, and the burst of the leading-edge vortex provides more nose-up moment. Among  $AOAs$  of  $18^\circ$  and  $30^\circ$ , the enhancement of the back-flow vortex goes higher, so that leads to the more nose-down moment. Then the vortex becomes weaker, and the burst of the leading-edge vortex takes the upper hand, so the nose-up moment comes bigger. Furthermore, even at  $AOA$  of  $37.5^\circ$ , the inner part of the ventral-opened configuration still provides nose-down moment.

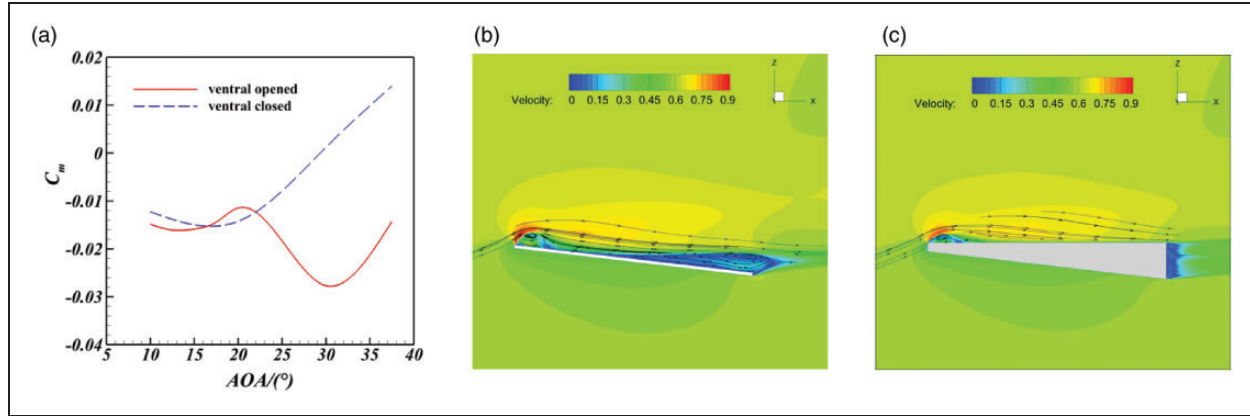
It can be seen from Table 2 that the inner parts of both configurations produce nose-up moment at the  $AOA$  of  $20^\circ$ , but the moment of the ventral-opened configuration (0.00065) is much smaller than the closed one (0.00256). Figure 10(b) and (c) presents the flow velocity distribution of the two configurations at the symmetrical plane at  $AOA = 20^\circ$ . Similar to the distribution at  $37.5^\circ$ , there is backflow vortex at the noses of the airplane for both configurations, which are far from reference points. It can provide a notable nose up moment, and the vortex on ventral-opened configuration is slightly bigger, and this can be explained by the bigger local  $AOA$ . However, a backflow appears near the trailing edge for the ventral-opened configuration, and this brings a great nose-down moment. It may explain why the nose-up moment of the ventral-opened configuration is much less than another configuration.

Both configurations have larger nose-up moment at  $AOA$  of  $37.5^\circ$  compared with that of  $20^\circ$ , and  $C_m$  of the ventral-closed configuration turns positive (0.01402) at this angle of attack. It can be seen that the nose-up moment is mainly generated by the outer wing. According to the spatial distribution of vorticity, we know that the burst location of the leading-edge vortex is very close to the leading edge when we have an  $AOA$  of  $37.5^\circ$ , resulting in the low-pressure zones moving forward, providing notable nose-up moment. However, the low-pressure caused by the back-flow vortex near the trailing edge can provide large nose-down moment for the ventral-opened configuration at this angle of attack. This may explain why the ventral-opened configuration can still remain negative  $C_m$  (−0.01431), and most of it



**Table 2.** Pitching moment coefficients by parts of the two configurations.

Alpha (°)	20			37.5		
Configuration	Open	Close	Difference	Open	Close	Difference
Inner part $C_m$	0.00065	0.00256	−0.00190	−0.02212	−0.00054	−0.02158
Outer part $C_m$	−0.01529	−0.01679	0.00150	0.00781	0.01456	−0.00675
Total $C_m$	−0.01463	−0.01423	−0.00040	−0.01431	0.01402	−0.02833

**Figure 10.** Pitching moment coefficient comparison and the spatial velocity distribution at  $AOA$  of  $20^\circ$ . (a) Pitching moment coefficient comparison for two configurations. (b) spatial velocity distribution on the asymmetrical plane for ventral-opened configuration. (c) spatial velocity distribution on the asymmetrical plane for ventral-closed configuration.

comes from the inner part. This benefit helps a lot when flying at high  $AOAs$  as it can make the paper plane stay stable, which is hard for a conventional airplane in such flying conditions.

## Conclusions

The flowfield on a paper plane with and without ventral gap was computed in present work, and the lift, drag, pitching moment, pressure and vortices distribution were examined in detail. The effect of the ventral gap was investigated with numerical methods. The following conclusions are made:

1. Compared with the configuration without ventral gap, the one with it can provide larger maximum  $C_L$  (1.49 vs 1.46), and also larger  $C_D$  because of the higher local  $AOA$  of the ventral gap and the back-flow vortices, resulting in a lower lift to drag ratio at  $AOAs$  among  $10\sim 42^\circ$ ;
2. The leading-edge vortex of ventral opened configuration breaks down faster than that of the other configuration, but the high-speed airflow of the ventral opened configuration is closer to the upper surface of the wing, and making it still gains larger lift;
3. At high  $AOAs$ , with the increase of the  $AOA$ , the vortex burst point moving forward to the leading edge makes the low-pressure area moving forward, too. This phenomenon leads to the increment of

the nose-up moment, and even makes the paper plane unstable for the ventral-closed configuration after  $AOA = 20^\circ$ , and the pitching moment coefficient becomes positive at  $37.5^\circ$ , which will make the paper plane nose up irreversibly. However, the ventral-opened configuration can still maintain nose down because of the ventral gap. The pitching moment coefficient is  $-0.01431$  compared with the ventral-closed configuration that has a value of  $0.01406$ . The inner part contributes  $-0.02212$  of pitching moment coefficient, and the outer part contributes to the nose-up moment.

4. Both configurations generate backflow vortex on the upper surface around the nose, which leads to nose-up moment, but only the ventral opened configuration will generate a second and larger backflow vortex before the trailing edge at high  $AOAs$ . This vortex brings higher  $C_L$ , and dramatic nose-down moment at high  $AOAs$ , as the vortex lies behind the center of gravity.

## Declaration of Conflicting Interests

The author(s) declared no potential conflicts of interest with respect to the research, authorship, and/or publication of this article.

## Funding

The author(s) disclosed receipt of the following financial support for the research, authorship, and/or publication

of this article: The authors acknowledge the support from the National Natural Science Foundation of China (grant no. 11602199), China Postdoctoral Science Foundation (grant no. 2017M623184) and the Fundamental Research Funds for the Central Universities (grant no. xzy012019064).

## References

1. Liu S and Qin N. Modelling roughness effects for transitional low Reynolds number aerofoil flows. *Proc IMechE, Part G: J Aerospace Engineering* 2015; 229: 280–289.
2. Genç MS, Özkan G, Özden M, et al. Interaction of tip vortex and laminar separation bubble over wings with different aspect ratios under low Reynolds numbers. *Proc IMechE, Part C: J Mechanical Engineering Science* 2018; 232: 4019–4037.
3. Mueller T and DeLaurier JD. An overview of micro air vehicle aerodynamics. *Progr Astronaut Aeronaut* 2001; 195: 1–10.
4. Azuma A. *The biokinetics of flying and swimming*. Reston, VA: American Institute of Aeronautics and Astronautics, 2006.
5. Shyy W, Lian Y, Tang J, et al. *Aerodynamics of low Reynolds number flyers*. New York, NY: Cambridge University Press, 2008.
6. Torres GE and Mueller T. Aerodynamic characteristics of low aspect ratio wings at low Reynolds numbers. *Progr Astronaut Aeronaut* 2001; 195: 115–141.
7. Gursul I. Review of unsteady vortex flows over slender delta wings. *J Aircraft* 2005; 42: 299–319.
8. Ng BF, Kng QM, Pey YY, et al. On the aerodynamics of paper airplanes. In: *27th AIAA applied aerodynamics conference*, San Antonio, Texas, 22–25 June 2009, p.3958.
9. Kegelman J and Roos F. Effects of leading-edge shape and vortex burst on the flowfield of a70-degree-sweep delta-wing. In: *27th Aerospace sciences meeting*, Reno, Nevada, 9–12 January 1989, p.86.
10. Dickinson MH and Gotz KG. Unsteady aerodynamic performance of model wings at low Reynolds numbers. *J Experiment Biol* 1993; 174: 45–64.
11. Mitchell AM and Détery J. Research into vortex breakdown control. *Progr Aerosp Sci* 2001; 37: 385–418.
12. Ol MV and Gharib M. Leading-edge vortex structure of nonslender delta wings at low Reynolds number. *AIAA J* 2003; 41: 16–26.
13. Torres GE and Mueller TJ. Low aspect ratio aerodynamics at low Reynolds numbers. *AIAA J* 2004; 42: 865–873.
14. Kwak D and Nelson R. Vortical flow control over delta wings with different sweep back angles using DBD plasma actuator. In: *5th Flow control conference*, Chicago, Illinois, 28 June–1 July 2010, p.4837.
15. Shen L, Wen C-y and Chen H-A. Asymmetric flow control on a delta wing with dielectric barrier discharge actuators. *AIAA J* 2016; 54: 652–658.
16. Schlüter JU. Aerodynamic study of the dart paper airplane for micro air vehicle application. *Proc IMechE, Part G: J Aerospace Engineering* 2014; 228: 567–576.
17. Menter FR. Two-equation eddy-viscosity turbulence models for engineering applications. *AIAA J* 1994; 32: 1598–1605.
18. Gan W and Zhang X. Design optimization of a three-dimensional diffusing S-duct using a modified SST turbulent model. *Aerosp Sci Technol* 2017; 63: 63–72.
19. Qiu Y, Bai J and Yalin LI. Study on influence of complex geometry details on the aerodynamic performance of high-lift system. *Acta Aeronautica Et Astronautica Sinica* 2012; 33(3): 421–429.
20. Kharoua N and Khezzar L. Large eddy simulation study of turbulent flow around smooth and rough domes. *Proc IMechE, Part C: J Mechanical Engineering Science* 2013; 227: 2686–2700.
21. Bai J, Liu N, Qiu Y, et al. The design of nacelle chine in large civil transport aircraft. *Acta Aerodynamica Sinica* 2014; 32: 190–196.
22. Traub LW, Moeller B and Rediniotis O. Low-Reynolds-number effects on delta-wing aerodynamics. *J Aircraft* 1998; 35: 653–656.